Geodetic imaging: reservoir monitoring using satellite interferometry

D. W. Vasco,[1] Charles Wicks Jr,[2] Kenzi Karasaki[3] and Osni Marques[4]

[1] *Berkeley Laboratory, University of California, Berkeley, CA, USA. E-mail: dwvasco@lbl.gov*
[2] *U.S. Geological Survey, Menlo Park, CA, USA*
[3] *Berkeley Laboratory, University of California, Berkeley, CA, USA*
[4] *National Energy Research Scientific Computing Center, Berkeley Laboratory, University of California, Berkeley, CA, USA*

SUMMARY

Fluid fluxes within subsurface reservoirs give rise to surface displacements, particularly over periods of a year or more. Observations of such deformation provide a powerful tool for mapping fluid migration within the Earth, providing new insights into reservoir dynamics. In this paper we use Interferometric Synthetic Aperture Radar (InSAR) range changes to infer subsurface fluid volume strain at the Coso geothermal field. Furthermore, we conduct a complete model assessment, using an iterative approach to compute model parameter resolution and covariance matrices. The method is a generalization of a Lanczos-based technique which allows us to include fairly general regularization, such as roughness penalties. We find that we can resolve quite detailed lateral variations in volume strain both within the reservoir depth range (0.4–2.5 km) and below the geothermal production zone (2.5–5.0 km). The fractional volume change in all three layers of the model exceeds the estimated model parameter uncertainty by a factor of two or more. In the reservoir depth interval (0.4–2.5 km), the predominant volume change is associated with northerly and westerly oriented faults and their intersections. However, below the geothermal production zone proper [the depth range 2.5–5.0 km], there is the suggestion that both north- and northeast-trending faults may act as conduits for fluid flow.

Key words: geodesy, inverse problems, satellite interferometry, surface displacement.

1 INTRODUCTION

When fluid is produced from or injected into the subsurface, it induces a volume change, which in turn deforms the Earth's surface. If the reservoir is horizontal and homogeneous, the resulting displacements will be distributed concentrically around the production/injection borehole. If a preferential flow path such as a fault zone exists, a frequent occurrence in many reservoirs, the flow will mostly occur along this pathway, and the distribution of volume change and subsequent surface displacements will be skewed. Therefore, the pattern of surface displacements can be used to make inferences about reservoir volume change. The distribution of volume change is tightly coupled to the spatial variation in reservoir permeability and compressibility, so that heterogeneities in volume change are directly related to lateral variations in these properties.

The surface expression of reservoir dynamics can be monitored by using high-precision tiltmeters (Evans *et al.* 1982), GPS, laser altimeters (Ridgway *et al.* 1997) and Interferometric Synthetic Aperture Radar [InSAR] (Zebker *et al.* 1994), depending on the magnitude of the displacements. A large number of measurement points are often needed to estimate reliably the distribution of reservoir volume changes. Monitoring of deformation at or near the surface costs very little compared to drilling a set of wells to reservoir depths and instrumenting them with pressure sensors. Recent technologies, such as InSAR, are able to provide very dense estimates of surface deformation at relatively low cost. Surface displacement observations provide independent data on reservoir dynamics that can be used to verify flow models based upon borehole data alone. Observations of surface deformation have proven useful in monitoring hydrofracturing (Evans *et al.* 1982; Castillo *et al.* 1997; Wright *et al.* 1998), fluid migration associated with volcanism (Vasco *et al.* 1988, 1990; Massonnet & Feigl 1995; Briole *et al.* 1997; Wicks *et al.* 1998; Dzurisin *et al.* 1999), steam injection (Bruno & Bilak 1994), well testing (Vasco *et al.* 1998) and petroleum production (Vasco *et al.* 2000).

In this paper we shall describe the use of InSAR observations to map changes in the state of a reservoir. That is, we develop and apply techniques for mapping InSAR range change data into volume changes within the reservoir. In many cases we may associate such volume change with pressure changes due to reservoir production. We pay particular attention to the calculation of resolution and uncertainty associated with the estimates. For example, we derive singular value decomposition (SVD) based assessment techniques for inverse problems with very general regularization. Using a Lanczos iteration scheme, we outline an approach which makes the calculation of resolution and covariance matrices feasible for inverse problems with very large data sets. The methodology is applied to a set of InSAR images from the Coso geothermal field.

2 METHODOLOGY

In this section we describe how the observed surface displacements may be used to infer the distribution of fractional volume change within the reservoir.

2.1 The equation governing static deformation in an elastic medium

The governing equation for displacements in an elastic medium, $u_i(\mathbf{x})$, $i = 1, 2, 3$, due to an internal strain is (Aki & Richards 1980, p. 19)

$$\frac{\partial}{\partial x_j}\left[\mu(\mathbf{x})\left(\frac{\partial u_i}{\partial x_j} + \frac{\partial u_j}{\partial x_i}\right)\right] + \frac{\partial}{\partial x_j}\left[\lambda(\mathbf{x})\frac{\partial u_k}{\partial x_k}\right]\delta_{ij} = f_i(\mathbf{x}) \tag{1}$$

where $f_i(\mathbf{x})$ is a source term,

$$f_i(\mathbf{x}) = -\frac{\partial}{\partial x_j}[K(\mathbf{x})\Psi(\mathbf{x})]\delta_{ij}. \tag{2}$$

The quantity $\Psi(\mathbf{x})$ is the stress-free volume strain, often denoted by $\Delta\theta$, given by

$$\Psi(\mathbf{x}) = \Delta e_{11} + \Delta e_{22} + \Delta e_{33}$$

where Δe_{11} are stress-free strain components (Aki & Richards 1980, p. 60). The relationship between the stress-free or transformational strain, which is the strain that a volume would undergo in the absence of the elastic matrix, and the constrained strain (strain in the presence of the matrix) is described in Eshelby (1957). The spatially varying functions $\mu(\mathbf{x})$, $\lambda(\mathbf{x})$ and $K(\mathbf{x})$ are the shear modulus, the Lame constant and the bulk modulus, respectively. In this work we invoke the Einstein summation convention in which we sum over repeated upper and lower indices.

There are several approaches one could take in order to solve eq. (1), depending on how well the medium is known. We might consider simplified elastic structures and solve the equation analytically. Examples of possible distributions of elastic properties are a homogeneous whole-space (Eshelby 1957), a homogeneous half-space (Mogi 1958; Maruyama 1964) and a layered half-space (Singh 1970; Jovanovich *et al.* 1974). Another approach extends this method by considering small perturbations of properties about one of these simple models (Du *et al.* 1994). The result is an equation for the displacement perturbations which may often be solved efficiently. Purely numerical techniques such as finite differences (Mitchell & Griffiths 1980; Vasco *et al.* 2000) or finite elements (Smith 1982) provide the most flexible methods for solving (1) given an arbitrary distribution of elastic properties. Such numerical techniques require more computational resources than the other approaches. However, because we are considering the static displacement problem, time stepping is not required and it is feasible to solve (1) numerically.

2.2 Green's function representation of the solution

In what follows we shall require the Green's function representation of the solutions of eq. (1). That is, we will need the functions $G_{in}(\mathbf{x}, \mathbf{y})$, $i, n = 1, 2, 3$ satisfying

$$\frac{\partial}{\partial x_j}\left[\mu\left(\frac{\partial G_{in}}{\partial x_j} + \frac{\partial G_{jn}}{\partial x_i}\right)\right] + \frac{\partial}{\partial x_j}\left[\lambda\frac{\partial G_{kn}}{\partial x_k}\right]\delta_{ij} = \delta_{in}\,\delta(\mathbf{x} - \mathbf{y}) \tag{3}$$

where $\delta_{in}\delta(\mathbf{x} - \mathbf{y})$ is a delta function source located at $\mathbf{y}$ with a non-zero nth component. Physically, $G_{in}(\mathbf{x}, \mathbf{y})$ represents the ith

component of displacement at $\mathbf{x}$ due to a point body force at $\mathbf{y}$ with non-zero component n. It is well known (Stakgold 1979; Aki & Richards 1980) that, given the solutions to (3), we may write the solution to (1) as the integral

$$u_n(\mathbf{x}) = \int_V f_i(\mathbf{y})G_{in}(\mathbf{x}, \mathbf{y})\,d\mathbf{y}. \tag{4}$$

Substituting the definition of $f_i(\mathbf{y})$ from eq. (2) produces

$$u_n(\mathbf{x}) = -\int_V \frac{\partial}{\partial y_i}[K(\mathbf{y})\Psi(\mathbf{y})]G_{in}(\mathbf{x}, \mathbf{y})\,d\mathbf{y}. \tag{5}$$

Because we are integrating over a volume containing the source and we may assume that $\Psi(\mathbf{y})$ vanishes at the integration boundaries, we may write (5) as

$$u_n(\mathbf{x}) = -\int_V K(\mathbf{y})\frac{\partial G_{in}(\mathbf{x}, \mathbf{y})}{\partial y_i}\Psi(\mathbf{y})\,d\mathbf{y}. \tag{6}$$

Defining the modified Green's function

$$g_n(\mathbf{x}, \mathbf{y}) = -K(\mathbf{y})\frac{\partial G_{in}(\mathbf{x}, \mathbf{y})}{\partial y_i} \tag{7}$$

we may write (6) as

$$u_n(\mathbf{x}) = \int_V g_n(\mathbf{x}, \mathbf{y})\Psi(\mathbf{y})\,d\mathbf{y}. \tag{8}$$

Thus, the nth component of displacement at point $\mathbf{x}$ is a scaled integral of the transformational volume strain within the reservoir. In the inverse problem we solve eq. (8) for the distribution $\Psi(\mathbf{y})$, given a discrete set of displacement observations, $u_n(\mathbf{x}_i)$.

A key component of this approach is the modified Green's function $g_n(\mathbf{x}, \mathbf{y})$ which appears in eq. (8). In the application described below, we implement an analytical solution for a uniform half-space, based upon a generalization of the results of Maruyama (1964), as described by Vasco *et al.* (1988). The modified Green's function is expressed as

$$g_n(\mathbf{x}, \mathbf{y}) = \frac{(\nu + 1)}{3\pi}\frac{(x_n - y_n)}{S^3} \tag{9}$$

where ν is Poisson's ratio and

$$S = \sqrt{(x_1 - y_1)^2 + (x_2 - y_2)^2 + (x_3 - y_3)^2} \tag{10}$$

is the distance from the source point to the observation point. This Green's function is appropriate for stress-free volume strain. When describing volume change constrained by the matrix, as in Mossop & Segall (1999), we must scale this function as describe by Eshelby (1957).

2.3 InSAR observations

InSAR, utilizing satellite-borne synthetic aperture radars, is a relatively recent development in observational geodesy (Zebker & Goldstein 1986). InSAR has been used to map topography (Zebker & Goldstein 1986), to image displacements induced by earthquakes (Massonnet *et al.* 1993; Zebker *et al.* 1994; Massonnet & Feigl 1995; Feigl *et al.* 1995; Murakami *et al.* 1996), to image deformation associated with magmatic systems (Massonnet & Feigl 1995; Briole *et al.* 1997; Wicks *et al.* 1998; Dzurisin *et al.* 1999) and to image ice dynamics (Goldstein *et al.* 1993; Fahnestock *et al.* 1993; Remy *et al.* 1999). InSAR has also proved useful in observing subsidence associated with mining (Carnec *et al.* 1996), geothermal production (Vadon & Sigmundsson 1997; Massonnet *et al.* 1997; Carnec & Fabriol 1999; Fialko & Simons 2000) and aquifer compaction

(Galloway *et al.* 1998; Hoffmann *et al.* 2001). We shall not concern ourselves with the details of extracting phase changes from satellite radar data. Information on this, with references, may be found in the recent review papers by Massonnet & Feigl (1998) and Bamler & Hartl (1998).

In the interferometric mode we measure phase changes, ϕ, between radar backscatter from the Earth's surface taken at various orbits of the satellite. The phase is related to the surface displacement projected onto the line of sight to the satellite by the expression (Zebker *et al.* 1994)

$$\phi = \frac{4\pi}{\lambda}(H + \Delta\rho) \tag{11}$$

where λ is the wavelength of the radar wave, H is the contribution from topography and $\Delta\rho$ is the change in distance to the satellite (range) that we seek. The effect of topography can be removed by using either a digital terrain model (DTM) or by using additional orbits to remove the topography term (Gabriel *et al.* 1989; Zebker *et al.* 1994). Removal of the topography using a DTM results in a range estimate which is accurate to 0.25–1.2 cm, for a nominal DTM error of 30 m. Using multiple satellite passes to remove topographic effects results in estimates which are accurate to a few millimetres (Zebker *et al.* 1994).

The basic datum in InSAR is the change in range over some time interval. If the surface of the Earth deforms during this period, the accumulated displacements of the imaging elements are projected onto the range vector, **l**, a unit vector which points toward the satellite. Thus,

$$\Delta\rho(\mathbf{x}) = \mathbf{u} \cdot \mathbf{l} = u_i l_i \tag{12}$$

where we are again invoking the summation convention for repeated indices. From eq. (8) we find that

$$\Delta\rho(\mathbf{x}) = \int_V r(\mathbf{x}, \mathbf{y})\Psi(\mathbf{y})\,d\mathbf{y} \tag{13}$$

where

$$r(\mathbf{x}, \mathbf{y}) = l_i g_i(\mathbf{x}, \mathbf{y}) \tag{14}$$

is the projection of the displacement Green's functions onto the range vector. The components of the vector **l** are known from the geometry of the satellites orbit. Note that, if different orbital geometries are available, it is possible to acquire different combinations of displacement components. For example, in our application at the Coso geothermal field, we use data from both the ascending and descending portions of the orbit to constrain subsurface volume strain better.

2.4 Estimation and assessment of reservoir fractional volume strain

2.4.1 Range change data, regularization and model parameter estimation

Discretization of the integral (13) is accomplished by expanding the distribution of reservoir fractional volume changes using a set of orthogonal basis functions e.g., Parker (1994). The basis set consists of the rectangular constant functions. We represent the volume strain in the reservoir by a finite number, M, of non-overlapping cells (Vasco *et al.* 1988, 2000). Each cell may undergo a distinct fractional volume change, say ν_j, for the jth cell. The contribution to the surface displacement from the volume strain in a single cell, $\Delta\rho^j(\mathbf{x})$, is given by

$$\Delta\rho^j(\mathbf{x}) = \nu_j \int_{V_j} r(\mathbf{x}, \mathbf{y})\,d\mathbf{y} \tag{15}$$

where V_j denotes the region occupied by cell j. The total fractional volume change in the reservoir is a summation over all M component cells. Hence, the accumulated range change at $\mathbf{x}_i$ is given by

$$\Delta\rho(\mathbf{x}_i) = \mathcal{R}_{ij}\nu_j \tag{16}$$

where

$$\mathcal{R}_{ij} = \int_{V_j} r(\mathbf{x}_i, \mathbf{y})\,d\mathbf{y} \tag{17}$$

and ν_j denotes the stress-free fractional volume change in cell j. Given a large number (N) of range change observations, at various points on the Earth's surface, we may solve the linear system of eq. (16) for the subsurface volume strain. A standard approach is to find the model parameters ν_j which minimize the sum of the squares of the residuals, leading to the well-known least-squares estimate (Parker 1994). At this juncture we shall normalize each equation by the estimated standard error of the associated datum. This normalization proves convenient later, when we estimate model parameter covariances. Denoting the standard error of the ith datum by σ_i, we scale the data $\Delta\rho(\mathbf{x}_i)$ and the coefficients $\mathcal{R}_{ij}$:

$$d_i = \frac{\Delta\rho(\mathbf{x}_i)}{\sigma_i} \tag{18}$$

$$\Gamma_{ij} = \frac{\mathcal{R}_{ij}}{\sigma_i}. \tag{19}$$

The weighted sum of the squares of the residuals is then given by

$$\Pi_d(\boldsymbol{\nu}) = \sum_{i=1}^{N} [d_i - \Gamma_{ij}\nu_j]^2. \tag{20}$$

One important consideration when solving for the volume strain is the conditioning of the eq. (16). In the case of InSAR data, the equations may be significantly over-determined and inconsistent. Even when the system is formally over-determined, trade-offs between parameters may render the system effectively underdetermined (Menke 1984). For example, there is often a trade-off between fractional volume changes at different depths (Dieterich & Decker 1975). To stabilize the inverse problem we shall include a roughness penalty as a regularization term. Such a term characterizes the spatial continuity of the volume strain, as measured by either the first or second spatial derivative (Menke 1984). In detail, the roughness penalty is of the form

$$\Pi_r(\boldsymbol{\nu}) = \sum_{i=1}^{M} (D_{ij}\nu_j)^2 = \nu_j S_{lj}\nu_l, \tag{21}$$

where

$$S_{lj} = D_{lk}D_{kj} \tag{22}$$

and D_{ij} is a linear differencing operator which approximates the spatial derivative operator. The inclusion of a roughness penalty makes precise the notion that the observed surface deformation is most likely due to a connected body rather than a collection of numerous isolated sources. We could easily include a norm penalty (damping) in addition to the roughness term. However, the truncation of singular values and singular vectors, introduced below, is roughly equivalent to a model norm penalty, as discussed in Menke (1984).

The penalized misfit is given by the sum

$$P(\boldsymbol{\nu}) = \Pi_{\mathrm{d}}(\boldsymbol{\nu}) + W_{\mathrm{r}}\Pi_{\mathrm{r}}(\boldsymbol{\nu}), \tag{23}$$

where W_r is a weighting factor determining the relative importance of the regularization with respect to the data misfit. The solution to the inverse problem is the volume strain distribution $\boldsymbol{\nu}$ which minimizes eq. (23). The necessary equations for a minimum of eq. (23) may be written in vector form (Tarantola 1987; Pratt & Chapman 1992)

$$[\boldsymbol{\Gamma}^{\mathrm{T}}\boldsymbol{\Gamma} + \mathbf{L}^{\mathrm{T}}\mathbf{L}]\boldsymbol{\nu} = \boldsymbol{\Gamma}^{\mathrm{T}}\mathbf{d}, \tag{24}$$

where $\mathbf{L} = W_{\mathrm{r}}^{1/2}\mathbf{D}$. Defining the $(N+M) \times M$ matrix

$$\mathbf{G} = \begin{bmatrix} \boldsymbol{\Gamma} \\ \mathbf{L} \end{bmatrix} \tag{25}$$

and

$$\mathbf{T} = \begin{bmatrix} \mathbf{d} \\ \mathbf{0} \end{bmatrix}, \tag{26}$$

we may write eq. (24) as

$$\mathbf{G}^{\mathrm{T}}\mathbf{G}\boldsymbol{\nu} = \mathbf{G}^{\mathrm{T}}\mathbf{T}. \tag{27}$$

If the product matrix $\mathbf{G}^{\mathrm{T}}\mathbf{G}$ in eq. (27) is invertible (non-singular) we may write the estimate of $\boldsymbol{\nu}$ as

$$\boldsymbol{\nu} = (\mathbf{G}^{\mathrm{T}}\mathbf{G})^{-1}\mathbf{G}^{\mathrm{T}}\mathbf{T}. \tag{28}$$

2.4.2 Assessment of the model parameter estimates

An essential part of an inverse problem entails assessing the uniqueness and uncertainty associated with the model parameter estimates. Formally, this is accomplished by constructing resolution and covariance matrices corresponding to the solution. As outlined in many texts (Aki & Richards 1980; Menke 1984; Tarantola 1987; Parker 1994), these measures may be constructed directly from the SVD of $\boldsymbol{\Gamma}$. For the augmented matrix, $\mathbf{G}$, in eqs (25) and (27) we must modify the derivation of the resolution and covariance matrices. That is, when non-diagonal regularization terms are included, such as those associated with roughness penalties, the conventional SVD representation of resolution as the matrix product $\mathbf{V}_p\mathbf{V}_p^{\mathrm{T}}$ (Aki & Richards 1980; Menke 1984) no longer holds. In the Appendix we derive the necessary modificaions.

Model parameter resolution. In terms of the SVD of $\mathbf{G}$ the resolution matrix is expressed as

$$\mathbf{R} = \mathbf{V}_{\mathrm{p}}\boldsymbol{\Upsilon}\mathbf{V}_{\mathrm{p}}^{\mathrm{T}}, \tag{29}$$

where

$$\boldsymbol{\Upsilon} = \mathbf{I} - \boldsymbol{\Lambda}_p^{-1}\mathbf{U}_{2p}^{\mathrm{T}}\mathbf{U}_{2p}\boldsymbol{\Lambda}_p, \tag{30}$$

as derived in the Appendix. The quantity $\mathbf{U}_2$ is associated with the lower M rows of the $(N+M) \times (N+M)$ matrix $\mathbf{U}$, which correspond to the regularization ($\mathbf{L}$). The matrix $\mathbf{R}$ constitutes the formal resolution matrix. Rows of $\mathbf{R}$ may be thought of as averaging or filtering coefficients which operate on the true parameters to produce an estimate. Deviations of $\mathbf{R}$ from an identity matrix indicate increased averaging or blurring.

Model parameter covariance. The model parameter covariance matrix, $\mathbf{C}_{\mathrm{m}}$, describes the uncertainties associated with the estimates. As outlined in the Appendix, for a problem in which the rows have been scaled by the standard errors, $\mathbf{C}_{\mathrm{m}}$ is given by,

$$\mathbf{C}_{\mathrm{m}} = \mathbf{V}_p\boldsymbol{\Omega}\mathbf{V}_p^{\mathrm{T}}, \tag{31}$$

where

$$\boldsymbol{\Omega} = \boldsymbol{\Lambda}_{\mathrm{p}}^{-2} - \boldsymbol{\Lambda}_{\mathrm{p}}^{-1}\mathbf{U}_{2\mathrm{p}}^{\mathrm{T}}\mathbf{U}_{2\mathrm{p}}\boldsymbol{\Lambda}_{\mathrm{p}}^{-1}. \tag{32}$$

There is a trade-off between model parameter resolution and model parameter covariance. For example, as the cut-off p is varied resolution may be increased or decreased with a corresponding increase or decrease in model parameter covariances. Thus, it is important to examine these measures in tandem when assessing a solution to the inverse problem.

3 APPLICATION: MONITORING PRODUCTION AT THE COSO GEOTHERMAL FIELD, CALIFORNIA

In this section we present an application of our methodology to field data. Specifically, we use InSAR data to estimate the production-induced fractional volume change, $\Psi(\mathbf{x})$, at the Coso geothermal field, California.

3.1 Geological, geothermal and geophysical setting

The Coso geothermal field is located at the southwestern margin of the Basin and Range province. It produces approximately 240 MW of electricity, making it the largest and most developed of the high temperature Basin and Range hydrothermal systems (Lutz *et al.* 1996). More than 100 wells define the production zone, ranging in depth from 0.4 to 2.5 km (Moore *et al.* 1989). The fluid temperatures within the field are quite high, values as large as 340°C have been measured at depths of less than 2.5 km (Moore *et al.* 1989).

The field lies at the confluence of three tectonic and structural regimes: the Basin and Range, the Sierra Nevada and the San Andreas–Garlock fault system (Wright 1976; Roquemore 1980). At least three sets of faults are mapped in the Coso volcanic field (Fig. 1) (Bacon *et al.* 1980; Roquemore 1980). Much of the volcanic and geothermal activity appears to be controlled by the orientations of these faults and fractures. For example, geothermal production is concentrated on a north-trending zone that passes through Devils Kitchen (Lutz *et al.* 1996). A second production zone is associated with a subparallel fault slightly to the east. The region between these faults is an area of low permeabilities with depressed near-surface temperatures (Lutz *et al.* 1996). The dominant host rock appears to be granitic plutons which are thought to be related to the Sierra Nevada batholith (Duffield *et al.* 1980). In addition, metamorphic and volcanic rocks are widely distributed throughout the region. Geophysical investigations (Plouff & Isherwood 1980; Young & Ward 1980; Reasenberg *et al.* 1980; Walter & Weaver 1980) support the presence of a small magma chamber 5–20 km below the Coso volcanic field. Local earthquake traveltime delays (Walck & Clayton 1987; Walck 1988) and shear wave amplitude attenuation (Sanders *et al.* 1988; Ho-Liu *et al.* 1988), suggest yet another low velocity, attenuating body, 3–5 km in depth and directly to the south of the Coso volcanics, beneath Indian Wells Valley.

3.2 InSAR observations at the Coso geothermal field

In an effort to better understand fluid flow in the Coso geothermal reservoir we examined surface displacements over a five year period, from 1992 to 1997 (Fig. 2). The displacement estimates were derived using SAR data from the ERS-1 satellite. The actual data consisted of
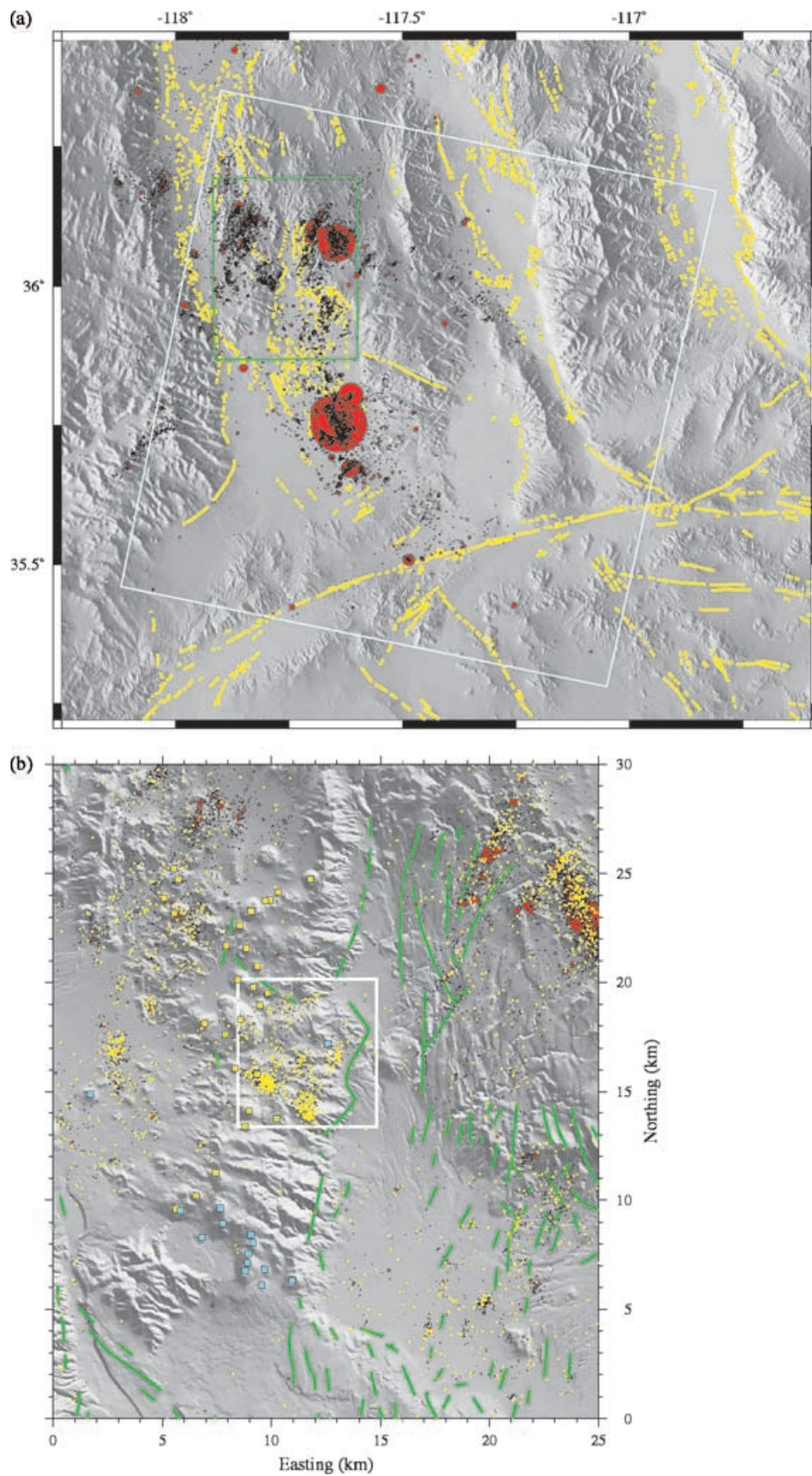
Figure 1. (a) Surface topography within and surrounding the Coso volcanic field. The area of study is indicated by the green rectangle. Inferred traces of regional faults are indicated by the yellow line segments. Regional seismicity is indicated by the filled red circles. The size of each circle is proportional to the earthquake magnitude. (b) Detailed topography in the study area. Mapped basalt and rhyolite domes are indicated by the yellow and blue squares. Mapped fault traces are denoted by the green line segments. Local seismicity is shown as yellow and red circles. The white rectangle denotes the location of the Coso geothermal production area.
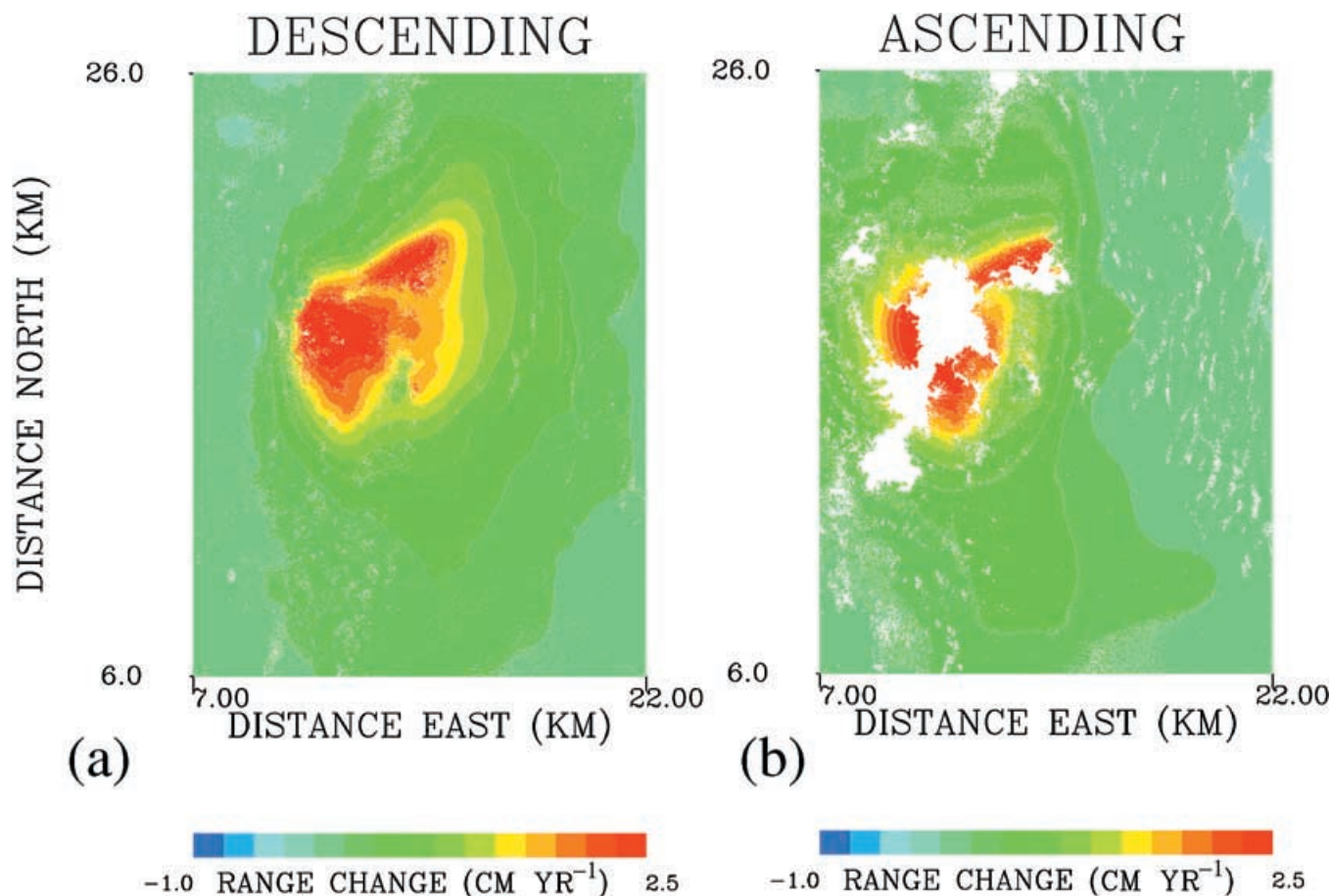
Figure 2. Map view of (a) the 325 375 descending orbit and (b) the 296 566 ascending range change rates that comprise our basic data set. The descending orbit estimates are a combination of range changes for five time intervals. A positive rate indicates an increase in distance between the satellite and that point on the Earth's surface. Subsidence over the time interval 1992–1997 maps into a positive range change. Discarded phase observations are indicated by white pixels in this figure.

range estimates from five pairs of descending satellite orbits (4/95–6/92, 5/96–9/93, 5/96–9/92, 9/96–6/92, 7/97–6/92) and a single pair of ascending satellite orbits (2/96–8/92).

Range changes associated with the descending orbits were converted to velocities (cm yr^{-1}) and averaged together to provide estimates of the overall velocity during the period 1997–1992. The pattern and magnitude of the velocities were very similar for all descending intervals, suggesting that the deformation was relatively constant from mid-1992 to mid-1997. Averaging over several time intervals should reduce the contamination by both atmospheric variations and satellite positioning errors. In addition, such averaging allows us to calculate sample variances associated with the estimates by examining the scatter about the mean velocities. The resulting average velocities are shown in Fig. 2(a). Note the dense sampling in Fig. 2(a), each pixel is 30 m by 30 m, for a total of 325 375 velocity estimates over the region.

The 296 566 velocity estimates from the single ascending orbit pair are shown in Fig. 2(b). As might be expected, the ascending orbit velocity estimates appear noisier than the averaged descending orbit velocity values. Also, there are significant regions in the geothermal field where, due to incoherence, we are simply unable to estimate range change. In these regions we have set the range change to zero, for display purposes only. Values from these regions are discarded and not used in the inversion described below. The

amplitude of the computed velocities from the ascending orbits is similar to estimates made using descending orbits. Also, the pattern is roughly similar to the that in Fig. 2(a). However, there are notable differences in detail between the descending and ascending velocity estimates.

Overall, the Coso geothermal field has undergone considerable surface displacement from 1992 to 1996, on the order of 2–3 cm yr^{-1}. The displacement appears as an increase in range that is, the distance from the satellite, during this period. Note the detailed structure contained in the map of descending range change. For example, there are at least three relative maxima in range change in Fig. 2(a). Also, there is an elongated, north-south zone of range increase in the centre of the figure.

3.3 Model assessment and estimates

The estimates of subsurface fractional volume change are based upon the inversion of the InSAR range measurements in Fig. 2. In particular, the subsurface volume strains are related to the range changes by eq. (13). The satellite look vector for the descending orbit, $\mathbf{l}_d$, has components (0.41, −0.08, 0.92) (east–west, north–south, vertical). For the ascending orbit the look vector components are $\mathbf{l}_a = (-0.35, -0.08, 0.93)$. In calculating the Green's function we assume that the elastic medium is a homogeneous

half-space, neglecting variations in topography and material properties. Ideally, we would account for the detailed variations in volcanic rocks in the subsurface. However, it is not possible to obtain an accurate distribution of lithology at Coso nor can we estimate the variation in elastic properties with any certainty. There are indications from seismic reflection studies that the Coso geothermal field in underlain by fairly uniform granitic material (Malin 1994).

Because of the irregular reservoir geometry, which consists of numerous intersecting faults, we chose simply to subdivide the entire region in Fig. 2 into a rectangular grid of cells. The dimensions of the grid are 19 (0.8 km) by 25 cells (0.8 km) in the east–west and north–south directions, respectively. In depth, the model consists of three layers, each of differing thickness. The first two layers roughly span the production interval (0.4–1.2 km and 1.2–2.5 km) of the Coso geothermal field. The lower layer 2.5–5.0 km is intended to model fractional volume changes below the geothermal field proper. This layer may be responding to geothermal production as well as capturing the behaviour of a possible hydrothermal–magmatic system underlying the geothermal field. In total, there are 1425 cells in the reservoir model. The volume strain distribution is constrained by the combined set of 62 1012 ascending and descending range change observations shown in Fig. 2.

Even though the inverse problem is formally over determined there are potential trade-offs between depth and volume strain which would introduce some degree of non-uniqueness. In order to stabilize the inverse problem we include a roughness penalty in the inversion. That is, we minimize the lateral roughness of the fractional volume change distribution in each layer, as given in eq. (21). Because we are only including three layers in our model we have not included a smoothing penalty in depth. Regularization of this type would minimize the differences between layers in the model. Such a penalty could prove useful for models with many layers. The penalty weight W_r used in the inversion is 0.00001, based upon an examination of the fit to the data produced by the inversion. That is, we pick W_r such that the data are neither significantly over-fit nor under-fit with respect to the estimated data errors. Additional regularization is provided by an SVD-based generalized inverse which incorporates a cut-off p, based upon the singular values associated with $\mathbf{G}$. In Fig. 3 we plot the spectrum of singular values associated with the matrix $\mathbf{G}$. We employed a cut-off of 1/500 of the peak value. That is, vectors $\mathbf{v}_i$ and $\mathbf{u}_i$ associated with λ_i less than 0.002 of the peak value are not used in calculating the generalized inverse, eq. (A2), nor are these vectors included in the computation of resolution or covariance, as given by eqs (29) and (31), respectively.

3.3.1 Model parameter resolution and covariance

In Fig. 4 we plot the diagonal of the model parameter resolution matrix, corresponding to the roughness penalty and the singular value cut-off of 1/500. Each diagonal element is plotted in its corresponding cell. The diagonal elements provide an overall measure of our ability to recover the volume strain in each cell. Values near 1.0 indicate that we are able to estimate the volume change in a specific cell with very little contribution from other parts of the model. Conversely, values near 0.0 signify substantial trade-off between the estimate and surrounding volume strain estimates. We see that cells in the top layer (0.4–1.2 km) are very well resolved, with values extremely close to 1. For the most part, the two deeper layers (1.2–2.5 and 2.5–5.0 km) are also well resolved, with values varying between 0.3 and 1.0. The most poorly resolved cells lie at the corners of the grid. The loss of resolution at the edges is most likely due to the fact that we have not included observations beyond the
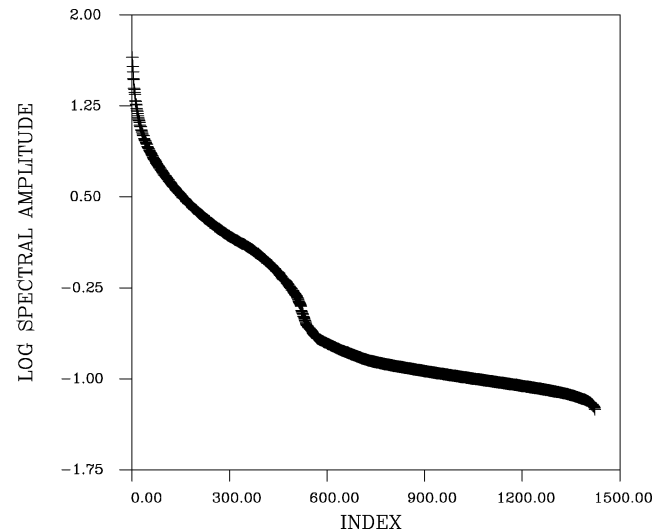

Figure 3. Spectrum of singular values associated with the matrix **G** in eq. (25).

boundaries of the inversion grid. By extending the set of observations beyond the grid we should improve the resolution in the two deeper layers. Note the extension of the well resolved cells in the east-west direction, particularly for the deepest layer (2.5–5.0 km). This is most likely due to our inclusion of observations from both ascending and descending orbits. The most significant difference between the descending orbit look vector, $\mathbf{l}_d = (0.41, -0.08, 0.92)$ and that of the ascending orbit, $\mathbf{l}_a = (-0.35, -0.08, 0.93)$, is in the first (east–west) component. Thus, we might expect that the combination of these two orbital geometries would improve the resolution in the east–west direction.

Additional insight is obtained if we examine a few rows of the resolution matrix. The elements of the ith row are averaging coefficients, which describe the contribution each component of volume strain makes to the estimate in the ith cell of our model. In Fig. 5 we present the averaging coefficients associated with a volume element located in the second layer of the model, the 788th row of the resolution matrix. Our resolution of the volume change in this cell is quite good, the diagonal component is 0.95 and there is little trade-off with estimates in the surrounding blocks. Similar results are obtained if we consider a block in the interior of the third layer, consider row 1243 of the resolution matrix (Fig. 6). The diagonal component is 0.99, very close to 1.0 and we observe essentially no trade-off in depth or within the layer. Thus, we find that we can reliably image volume changes over most of the inversion grid. In contrast, consider a block at the corner of the inversion grid, cell 1385, which is situated in the lowermost layer (Fig. 7). The diagonal component of resolution for this cell is 0.55 and we observe averaging within the layer of cells. The contributions from adjacent cells are both positive and negative in sign. The largest averaging coefficients have magnitudes of -0.15 and correspond to cells to the northeast and to the south-west of grid block 1385 (Fig. 7). There also appears to be somewhat more averaging in the north–south direction, perhaps reflecting the contribution of the descending and ascending orbits in constraining the volume strain model. In summary, it appears that the distribution of range change data with respect to the grid boundaries and the orbital geometries are contributing to the variations in model parameter resolution.

In computing the covariance matrix we first normalized the inverse problem by scaling each equation by the standard error of
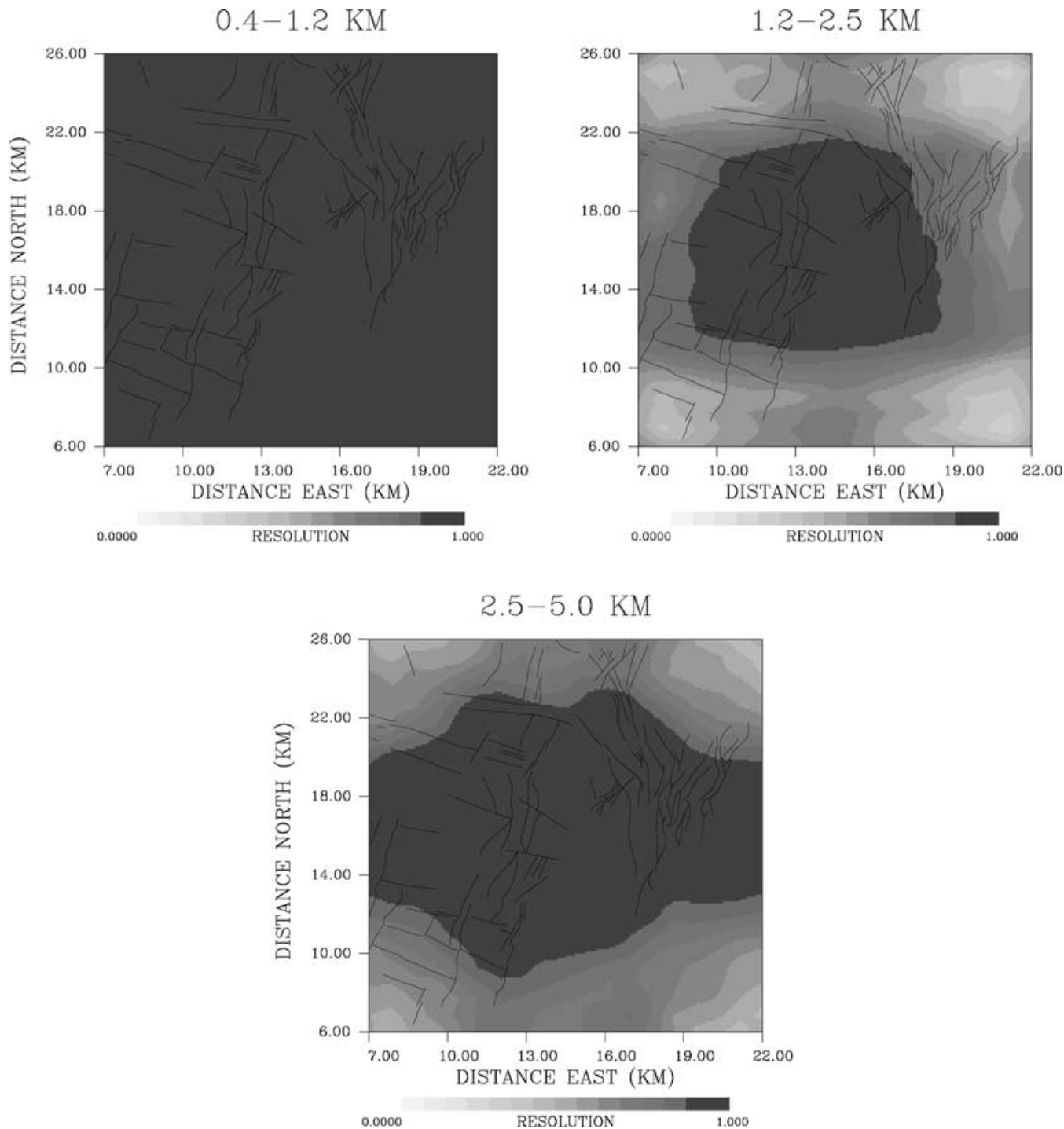
Figure 4. Diagonal elements of the resolution matrix **R**, computed using the Lanczos algorithm and the SVD representation of eq. (29). Each element has been plotted at the position of its associated block.

the particular data value (eqs 18 and 19). For the descending orbit data, the errors were computed from the scatter between the five orbital estimates. A base error of 0.5 cm yr^{-1} was provided for those averages with anomalously low scatter. For the ascending orbit pair we used the average error derived from the descending orbit data, scaled by the square root of the number of descending orbit pairs (to account for the averaging). In Fig. 8 the estimates of model parameter standard error are shown. Overall, the estimated errors are

less than 0.15×10^{-4}, increasing with depth from the surface. The error estimates are important when examining the significance of fractional volume changes in the model.

3.3.2 Estimates of fractional volume change

We used an iterative technique to generate the solution of the penalized least-squares problem. The resulting distribution of reservoir

0.4−1.2 KM

1.2−2.5 KM

2.5−5.0 KM
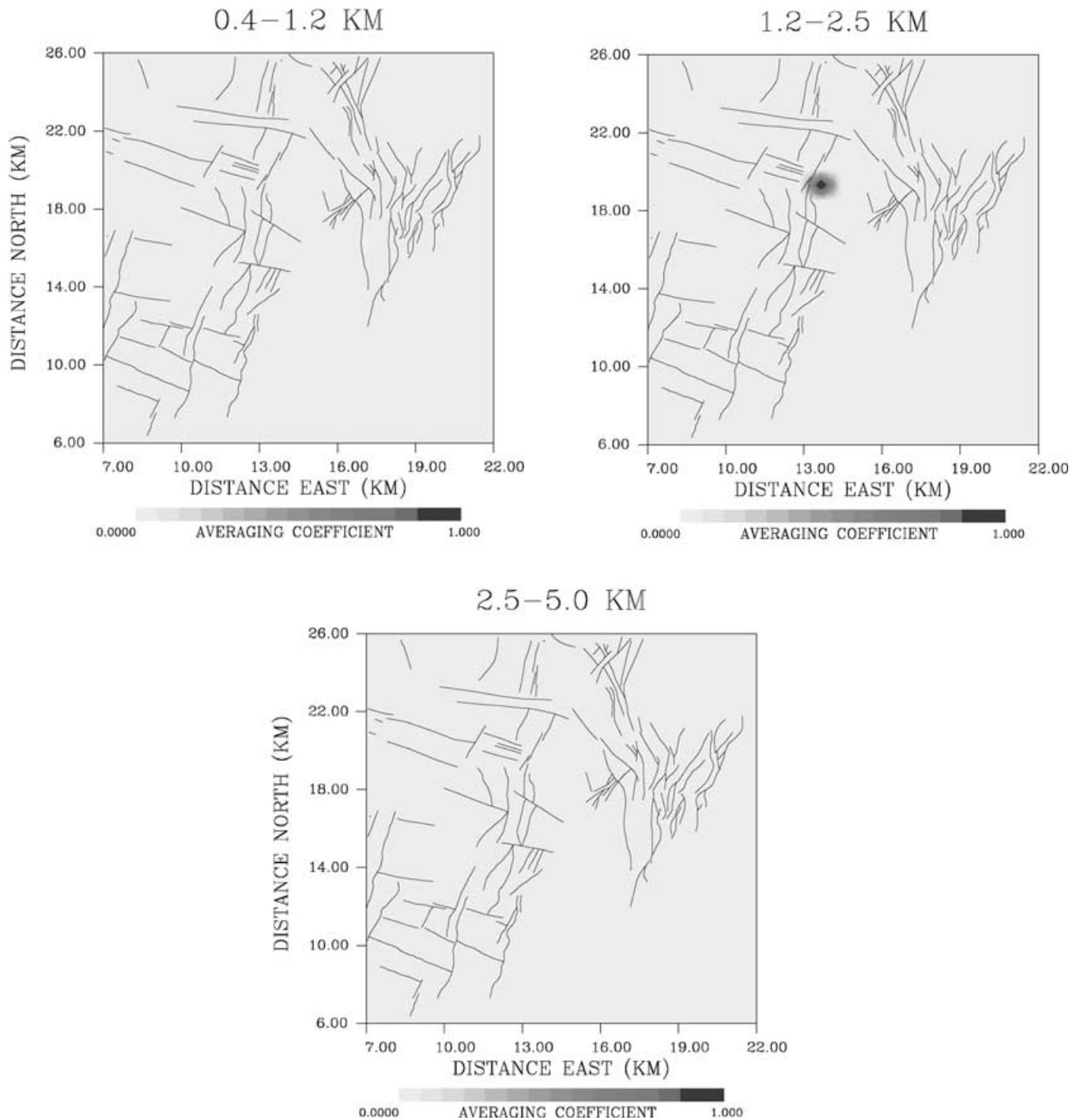
Figure 5. The 788th row of the resolution matrix. This block is roughly at the centre of the second layer (1.2–2.5 km). The grey scale indicates the relative contribution made by each model parameter to the estimate of volume change in block 788.

volume change is shown in Fig. 9 for the three layers of the model. The pattern of volume change in the uppermost layer (0.4–1.2 km) is quite intricate, with the largest anomalies associated with regions of geothermal production. For example, a peak volume change of over 1.5×10^{-4} is found beneath the primary production zone. The largest volume decreases seem to lie at, or near, north- and west-trending faults and their intersections. There are isolated volume decreases both to the east and to the north of the primary geothermal production zone. These anomalies appear to be significant, the magnitudes

exceed the model parameter uncertainties (Fig. 8). The northernmost volume decrease, which underlies the Coso Hot Springs, appears to be disconnected from the largest anomaly in this depth interval.

At depth, but still within the geothermal field (1.2–2.5 km), the largest volume decrease also coincides with the primary production zones. This peak volume decrease underlies a west-trending fault and occurs just to the east of Sugarloaf Mountain. We find a slight elongation of the peak anomaly along the fault trend. However, there
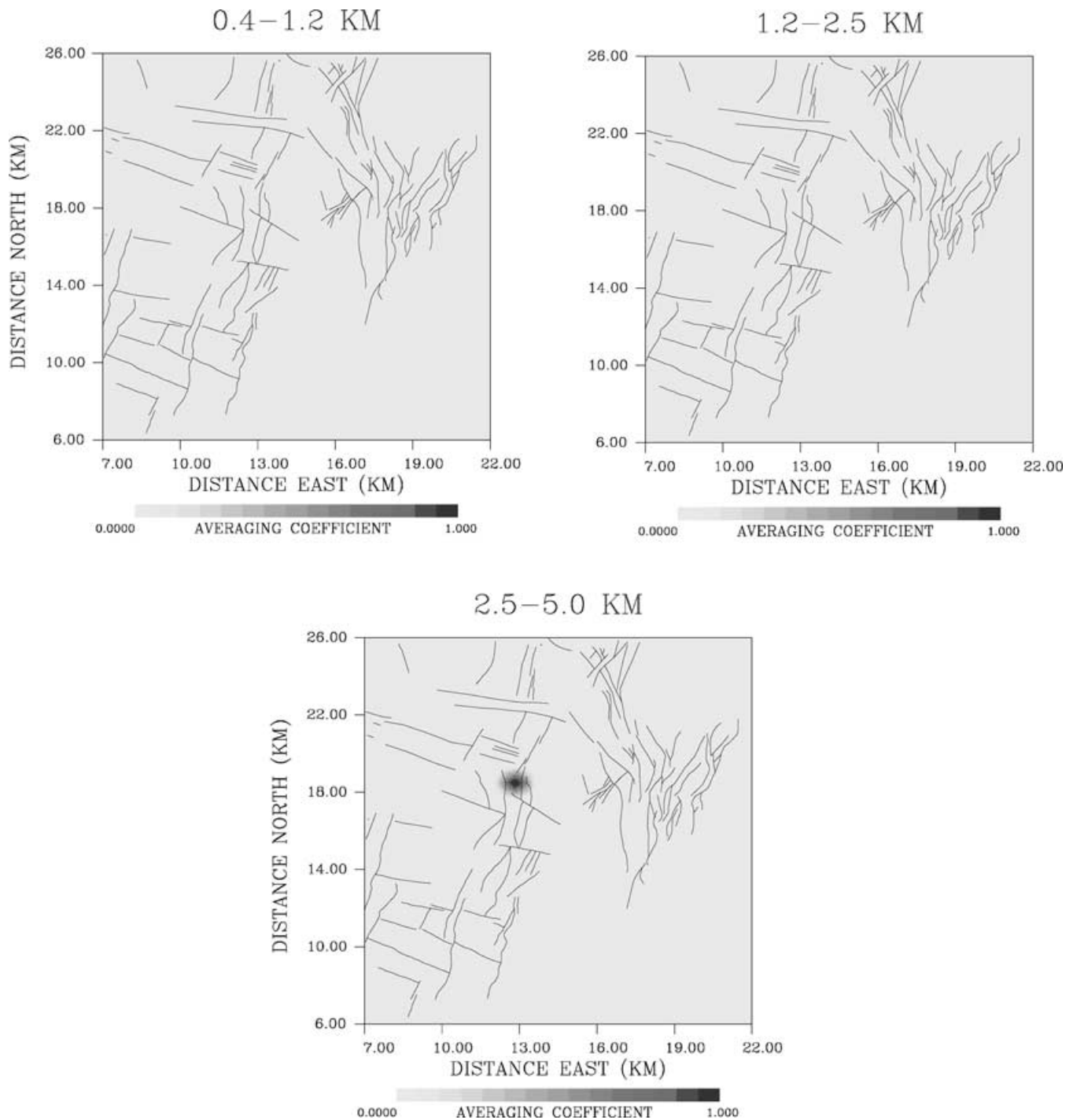
0.4–1.2 KM

1.2–2.5 KM

2.5–5.0 KM

Figure 6. The 1243th row of the resolution matrix. This block lies in the third layer (2.5–5.0 km).

is also a component of volume change extending to the south of the peak anomaly. There is an additional, roughly linear, trend of volume change associated with the northeast portion of the geothermal field. This part of the field underlies Coso Hot Springs. It is not clear if this volume decrease constitutes a disconnected part of the reservoir in this depth range.

In the deepest interval (2.5–5.0 km) the peak fractional volume decrease is oriented to the northeast. The anomaly extends from

just to the southeast of Sugarloaf Mountain to beneath Coso Hot Springs. The trend of this anomaly parallels the northeast trending faults mapped on the surface (Duffield *et al.* 1980). There is also some elongation of the fractional volume decrease in the north–south direction, particularly to the north of the production zone. Unfortunately, the resolution degrades at the northernmost edge of the grid and we cannot completely constrain this portion of the model. In particular, there may be some degree of north–south
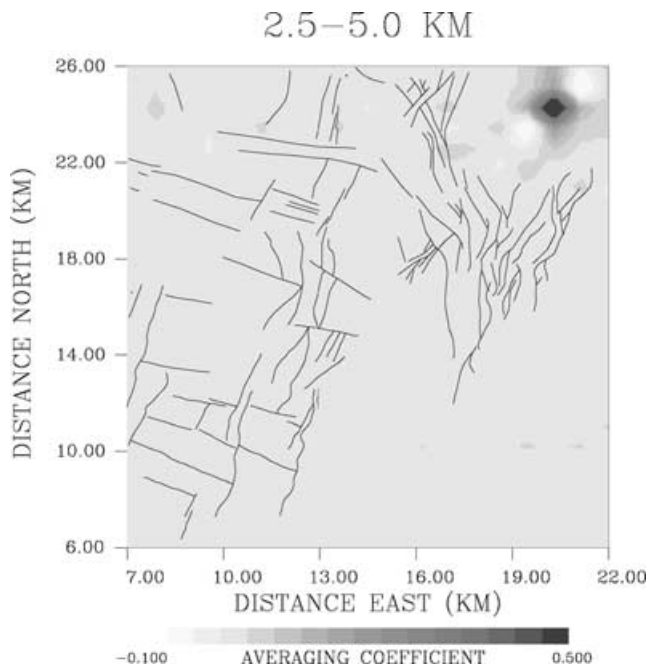
2.5–5.0 KM

Figure 7. The 1,385th row of the resolution matrix. This block lies in the third layer (2.5–5.0 km) near the northeast corner of the grid. In this figure only volume changes in the third layer are shown.

averaging at the northern edge, as in Fig. 7. By including additional observations beyond the inversion grid we should be able to improve the resolution in this region.

The fractional volume change in the 1425 cells of the model produces a reasonable fit to the 325 375 descending and the 296 566 ascending orbit data (Fig. 10). Most observations are fitted to within 1.0 standard error and all observations are fit to within 1.5 standard errors. This suggests that we may have overestimated the error in our data somewhat or that the data are not all independent. For a normal distribution we expect that around 5 per cent of the data would exceed 2σ. Note that the signal-to-noise ratio is lower overall for the ascending data. These data are derived from a single pair of orbits, in contrast to the descending orbit estimates, which are averages over five pairs. Hence, there is considerably more scatter in the ascending orbit values and the estimates of their standard deviations are correspondingly higher. Given the possible errors in the data, due to atmospheric and topographic variations and the simplifying assumptions in the model, the fit to both sets of measurements seems acceptable.

3.4 Interpretation

It is interesting to examine features of the inversion result in light of previous geological and geophysical investigations at Coso. The location of significant volume change near north- and west-trending faults and their intersections agrees with previous observations. In particular, the mapped faults in the region are thought to control fluid flow in the geothermal reservoir. Recent travel-time tomography studies (Wu & Lees 1999; Lees & Wu 1999) suggest a complicated distribution of seismic velocities and a significant variation in seismic anisotropy above 4 km in depth. The distribution of microseismicity also implies substantial heterogeneity in the seismically active upper 4 km (Walter & Weaver 1980; Feng & Lees 1998). Such complexity is mirrored in the distribution of fractional volume changes within the upper

layer (0.4–1.2 km) of the model (Fig. 9). A recent interpretation of InSAR observations over the Coso geothermal field has produced similar patterns of volume change in the subsurface (Fialko & Simons 2000). For example, they find that the InSAR observations can be largely explained by volume changes in the depth range 1–3 km. Similarly, we find that the largest components of volume change are located in the two uppermost layers 0.4–2.5 km in depth. Also, the orientations of the deformation sources of Fialko & Simons (2000) share common orientations with our patterns: a shallow (approximately 1 km depth), east-northeast-trending volume increase and a deeper (3.1 km) and larger north-northeast-trending body. There are differences between the solutions as well which may be due to differences in our approaches as well as in our data sets.

One surprising feature of the volume strain model is the occurrence of a rather linear, northeasterly oriented volume decrease 2.5–5.0 km in depth. This deeper anomaly is interesting because it is located above the low-velocity anomaly noted by Reasenberg *et al.* (1980). The northeast end of this anomaly is directly beneath the Coso Hot Springs. Furthermore, there is evidence from both teleseismic tomography at Coso (Reasenberg *et al.* 1980) and geochemistry (Manley & Bacon 2000) that the top of a magmatic body may lie just below a depth of 5 km. The absence of substantial earthquake activity below 5 km suggests a brittle–ductile transition as might be associated with such a magmatic body. Thus, the fractional volume decrease at the base of the model may be associated with a mass transfer of fluids related to a more deeply emplaced magma body. The northeast orientation of the fractional volume change anomaly is also interesting. This direction parallels the trend of a set of mapped surface faults (Hulen 1978; Duffield *et al.* 1980). Also, seismicity patterns and focal mechanisms surrounding the geothermal area suggest both right-lateral motion along northwest-striking planes and conjugate northeast left-lateral strike-slip motion (Walter & Weaver 1980). Within the field itself north-northeast normal-faulting mechanisms predominate. Overall, the focal mechanisms are consistent with north–south compression and east-west extension (Walter & Weaver 1980). Both 3-D *P* and *S* velocity tomography results (Wu & Lees 1999) and the 3-D distribution of seismic anisotropy (Lees & Wu 1999) support a northeast fast direction, an indication of local fault and fracture orientations, beneath Coso Hot Springs. Such northeast-trending faults and fractures agree with the fractional volume change pattern. Combined chemical analysis of the fluids and fluid inclusion measurements indicate a general migration of high temperature fluids from a deeper source in the southern part of the geothermal field (Moore *et al.* 1989; Lutz *et al.* 1996). The thermal plume migrates upwards towards the north and east through the fractured host rock (Moore *et al.* 1989). Such fluid migration is compatible with the model of fractional volume change (Fig. 9). As a final point, we note that the pattern of fractional volume change in Fig. 9 (2.5–5.0 km) contains a long wavelength signal which is oriented roughly north–south to north-northeast, following the trend of mapped normal faults in the region. Thus, these faults also appear to play a role in the deep large-scale fluid movement at Coso.

4 CONCLUSIONS

Observable surface deformation has been associated with mining, volcanic deformation, faulting, hydrofracturing, fluid movement into and out of aquifers, oil field operations and geothermal production. Even sources several kilometres deep have been shown to generate measurable surface displacement. In general, such deformation has not been fully utilized to infer reservoir
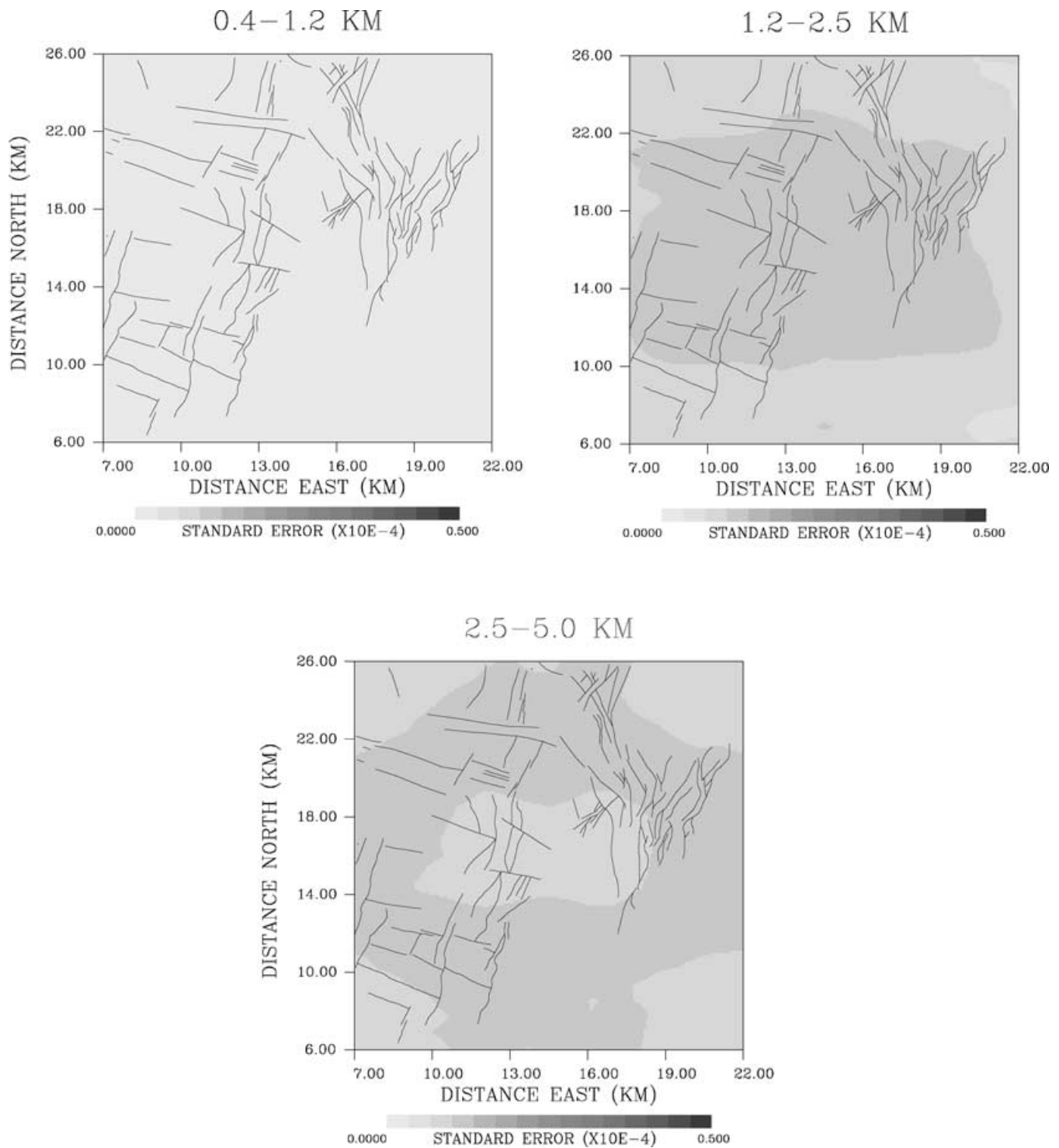
Figure 8. Model parameter standard error estimates derived from the covariance matrix. The covariance matrix was computed using eq. (31) and the Lanczos algorithm. The standard errors are the square roots of the diagonal elements of the covariance matrix. As in Fig. 4, we have plotted the values at the position of the blocks to which they correspond.

dynamics. As demonstrated in this paper, we can gain important insights into reservoir processes through the use of surface displacements. In particular, we may image fluid migration along faults or fractures in the subsurface. Recent innovations such as borehole tiltmeters, relative Global Positioning System (GPS) networks and Interferometric Synthetic Aperture Radar (InSAR) promise to

extend observational capabilities in a number of ways. For example, both borehole tiltmeters and GPS networks provide dense temporal sampling of surface displacements. InSAR provides almost continuous spatial coverage of large regions of the Earth's surface at low cost. There are advantages in combining several of these technologies to better constrain subsurface processes. For
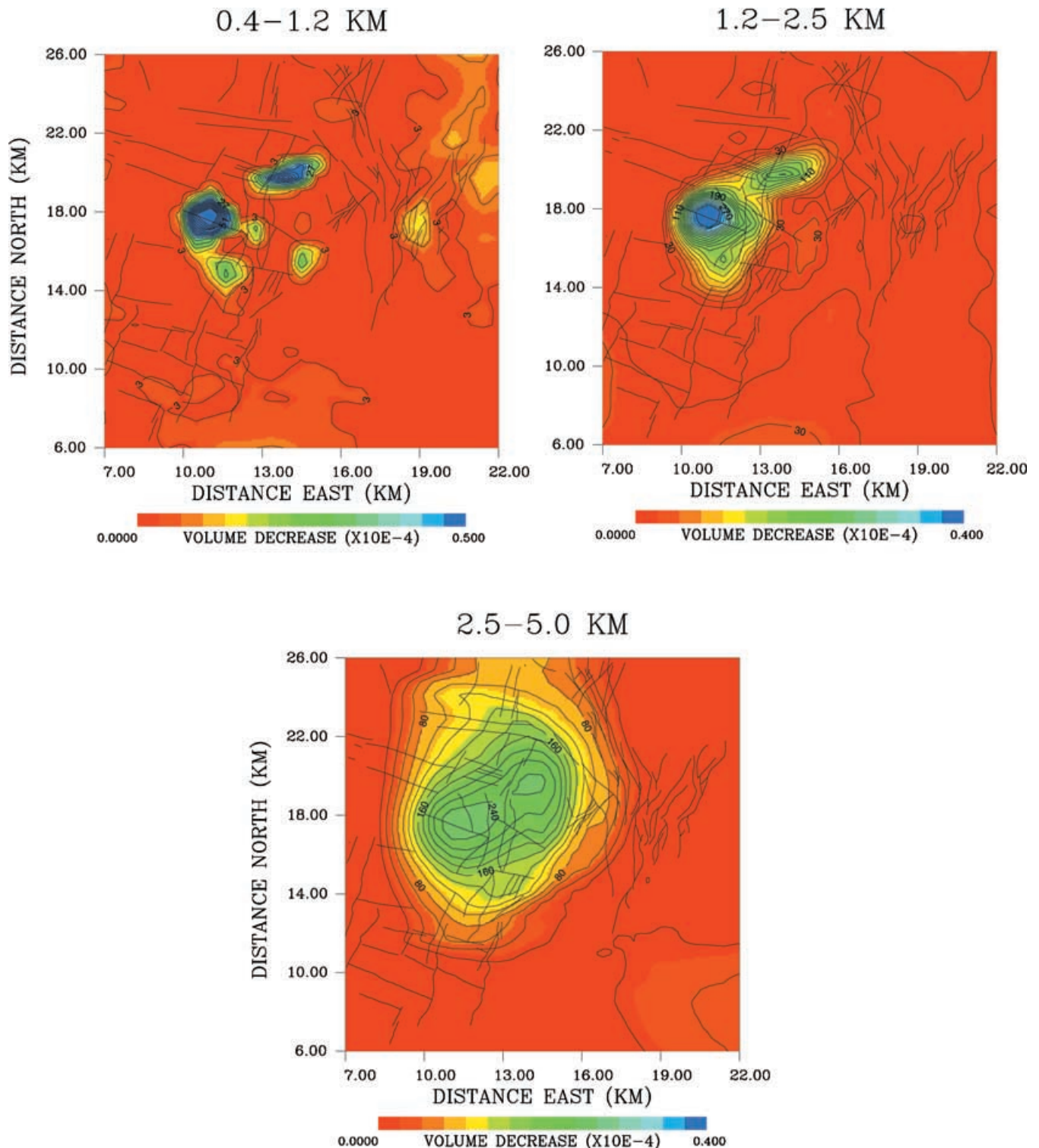
Figure 9. Stress-fress volume strain estimates for the three layers of the model. The colour scale is a unitless measure of fractional volume change (volume strain). The solid lines indicate mapped faults, taken from Duffield *et al.* (1980). Note that the faults shown here are only a subset of those in Duffield *et al.* (1980).

example, GPS provides three components of displacement while InSAR observations are a weighted sum of the displacement components. It has been demonstrated that the use of all components of displacement can better constrain subsurface volume change (Dieterich & Decker 1975). Therefore, it makes sense to combine

InSAR data, with its dense spatial coverage, with three-component GPS data.

Surface deformation data are sensitive to the dynamics of reservoir processes. That is, it measures changes over time rather than static quantities. Thus, it is somewhat like transient pressure
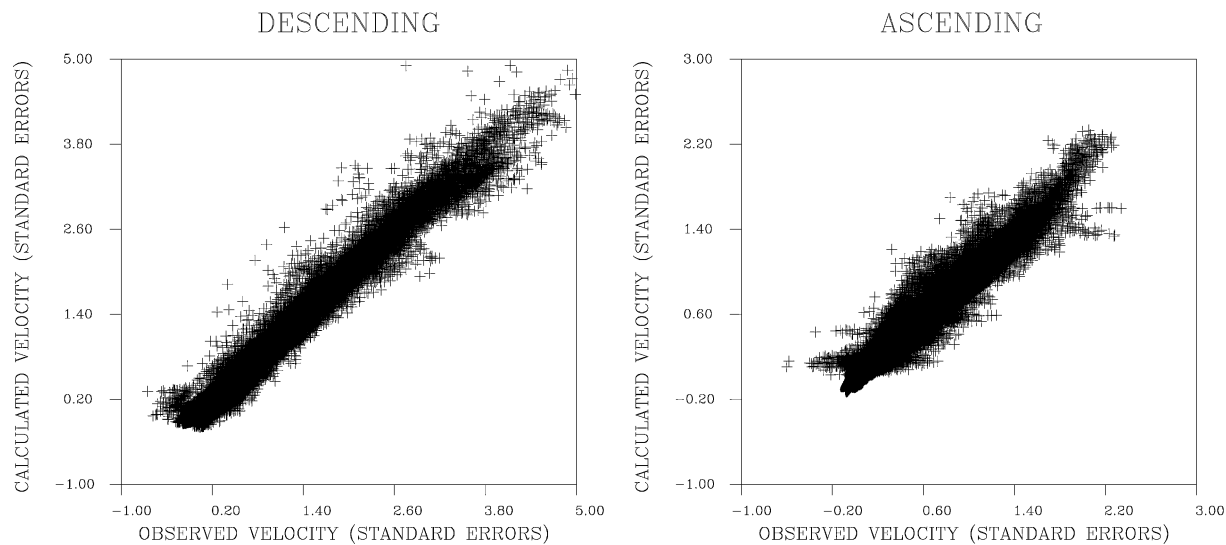
DESCENDING

ASCENDING

Figure 10. Observed range changes and range changes predicted by the model of volume strain (Fig. 9). The data are scaled by their estimated standard errors.

observations in boreholes, sensing the temporal variation in the state of a reservoir. It would be interesting to couple surface deformation observations with other dynamic reservoir data such as transient pressure, tracer and multiphase flow data.

Like many other geophysical measurements made at the Earth's surface, there are limitations in our ability to resolve volume changes in depth. Therefore, it is particularly important to calculate model parameter resolution and covariance. We have shown how this may be accomplished for large linear inverse problems with fairly general regularization. Using these methods we found that we are able to discern important variations in depth. Given sufficient information about the reservoir geometry it is possible to provide even sharper constraints on the 3-D variations in volume change. For example, if the reservoir is defined by known boundaries we may resolve more detailed variations in fractional volume change, or if fluid flow is confined to a set of known faults we can better constrain the reservoir volume changes laterally and in depth. Also, if the geometry of the faults are known we can tailor our dislocation source to represent the opening of a narrow fracture zone better. For example, we could represent the opening of an extensional crack by a strain nucleus W_{11} (Maruyama 1964) rather than by an array of volume changes as we have done here.

ACKNOWLEDGMENTS

REFERENCES

Aki, K. & Richards, P.G., 1980. *Quantitative Seismology,* Freeman & Sons, San Francisco.

Bacon, C.R., Duffield, W.A. & Nakamura, K., 1980. Distribution of Qua-ternary rhyolite domes of the Coso Range, California: Implications for extent of the geothermal anomaly, *J. geophys. Res.,* **85,** 2425–2433.

Bamler, R. & Hartl, P., 1998. Synthetic aperture radar interferometry, *Inverse Problems,* **14,** R1–R54.

Briole, P., Massonnet, D. & Delacourt, C., 1997. Post-eruptive deformation associated with the 1986–1987 and 1989 lava flows of Etna, detected by radar interferometry, *Geophys. Res. Lett.,* **24,** 37–40.

Bruno, M.S. & Bilak, R.A., 1994. Cost-effective monitoring of injected steam migration using surface deformation analysis, *Proc. SPE West. Reg. Mtg., Long Beach, CA,* **27888,** 397–412.

Carnec, C. & Fabriol, H., 1999. Monitoring and modeling land subsidence at Cerro Prieto geothermal field, Baja California, Mexico, using SAR interferometry, *Geophys. Res. Lett.,* **26,** 1211–1214.

Carnec, C., Massonnet, D. & King, C., 1996. Two examples of the use of SAR interferometry on displacement fields of small spatial extent, *Geophys. Res. Lett.,* **23,** 3579–3582.

Castillo, W., Hunter, S., Harben, P., Wright, C., Conant, R. & Davis, E., 1997. Deep hydraulic fracture imaging: Recent advances in tiltmeter technologies, *Int. J. Rock. Mech. Min. Sci.,* **34,** 3–4.

Dieterich, J.H. & Decker, R.W., 1975. Finite element modeling of surface deformation associated with volcanism, *J. geophys. Res.,* **80,** 4094–4102.

Du, Y., Segall, P. & Gao, H., 1994. Dislocations in inhomogeneous media via a moduli perturbation approach: General formulation and two-dimensional solutions, *J. geophys. Res.,* **99,** 13 767–13 779.

Duffield, W.A. & Bacon, C.R., 1980. Geologic map of the Coso volcanic field and adjacent areas, Inyo County, California, *Misc. Geol. Invest.* Map I-1200, scale 1:50,000, USGS, Menlo Park, Calif.

Duffield, W.A., Bacon, C.R. & Dalrymple, G.B., 1980. Late Cenozoic volcanism, geochronology and structure of the Coso Range, Inyo County, California, *J. geophys. Res.,* **85,** 2381–2404.

Dzurisin, D., Wicks, C. & Thatcher, W., 1999. Renewed uplift at the Yellowstone Caldera measured by leveling surveys and satellite radar interferometry, *Bull. Volcanol.,* **61,** 349–355.

Eshelby, J.D., 1957. The determination of the elastic field of an ellipsoidal inclusion and related problems, *Proc. R. Soc. Lond.,* A., **241,** 376–396.

Evans, K.F., Holzhausen, G.R. & Wood, M.D., 1982. The geometry of a large-scale nitrogen gas hydraulic fracture formed in Devonian shale: An example of fracture mapping using tiltmeters, *SPE J.,* **22,** 755–763.

Fahnestock, M.A., Bindschadler, R., Kwok, R. & Jezek, K., 1993. Greenland ice sheet surface properties and ice dynamics from ERS-1 synthetic aperture radar imagery, *Science,* **262,** 1530–1534.

Feigl, K.L., Sergent, A. & Jacq, D., 1995. Estimation of an earthquake focal mechanism from a satellite radar interferogram: Application to the December 4, 1992 Landers aftershock, *Geophys. Res. Lett.,* **22,** 1037–1038.

Feng, Q. & Lees, J.M., 1998. Microseismicity, stress and fracture in the Coso geothermal field, California, *Tectonophysics,* **289,** 221–238.

Fialko, Y. & Simons, M., 2000. Deformation and seismicity in the Coso geothermal area, Inyo County, California: Observations and modelling using satellite radar interferometry, *J. geophys. Res.,* **105,** 21 781–21 793.

Gabriel, A.K., Goldstein, R.M. & Zebker, H.A., 1989. Mapping small elevation changes over large areas: Differential radar interferometry, *J. geophys. Res.,* **94,** 9183–9191.

Galloway, D.L., Hudnut, K.W., Ingebritsen, S.E., Phillips, S.P., Peltzer, G., Rogez, F. & Rosen, P.A., 1998. Detection of aquifer system compaction and land subsidence using interferometric synthetic aperture radar, Antelope Valley, Mojave Desert, California, *Water Resour. Res.,* **34,** 2573–2585.

Goldstein, R.M., Engelhardt, H., Kamb, B. & Frolich, R.M., 1993. Satellite radar interferometry for monitoring ice sheet motion: Application to an Antarctic ice stream, *Science,* **262,** 1525–1530.

Golub, G.H. & Van Loan, C.F., 1989. *Matrix Computations,* Johns Hopkins University Press, Baltimore.

Hoffmann, J., Zebker, H.A., Galloway, D.L. & Amelung, F., 2001. Seasonal subsidence and rebound in Las Vegas Valley, Nevada, observed by synthetic aperture radar interferometry, *Water Resour. Res.,* **37,** 1551–1566.

Ho-Liu, P., Kanamori, H. & Clayton, R.W., 1988. Applications of attenuation tomography to Imperial Valley and Coso-Indian Wells Region, Southern California, *J. geophys. Res.,* **93,** 10 501–10 520.

Hulen, J.B., 1978. Geology and alteration of the Coso geothermal area, Inyo County, California, *Rept, Univ. Utah Res. Inst. Earth Sci. Lab.,* Salt Lake City.

Jovanovich, D.B., Husseini, M.I. & Chinnery, M.A., 1974. Elastic dislocations in a layered half-space—I. Basic theory and numerical methods, *Geophys. J. R. astr. Soc.,* **39,** 205–217.

Lanczos, C., 1950. An iterative method for the solution of the eigenvalue problem of linear differential and integral operators, *J. Res. Nat. Bur. Stand.,* **45,** 255–282.

Lees, J.M. & Wu, H., 1999. P wave anisotropy, stress and crack distribution at Coso geothermal field, California, *J. geophys. Res.,* **104,** 17 955–17 973.

Lutz, S.J., Moore, J.N. & Copp, J.F., 1996. Integrated mineralogical and fluid inclusion study of the Coso Geothermal System, California, 21st Workshop on Geothermal Reservoir Engineering, pp. 187–194, Stanford University.

Malin, P., 1994. The seismology of extensional hydrothermal systems, *Trans. Geotherm. Resour. Counc.,* **18,** 17–22.

Manley, C.R. & Bacon, C.R., 2000. Rhyolite thermobarometry and the shallowing of the magma reservoir, Coso Volcanic Field, California, *J. Petrol.,* **41,** 149–174.

Maruyama, T., 1964. Statical elastic dislocations in an infinite and semi-infinite medium, *Bull. Earth. Prev. Res. Inst. Univ. Tokyo,* **42,** 289–368.

Massonnet, D. & Feigl, K., 1995. Discriminating geophysical phenomena in satellite radar interferograms, *Geophys. Res. Lett.,* **22,** 1537–1540.

Massonnet, D. & Feigl, K., 1998. Radar interferometry and its application to changes in the Earth's surface, *Rev. Geophys.,* **36,** 441–500.

Massonnet, D., Rossi, M., Carmona, C., Adragna, F., Peltzer, G., Feigl, K. & Rabaute, T., 1993. The displacement field of the Landers earthquake mapped by radar interferometry, *Nature,* **364,** 138–142.

Massonnet, D., Briole, P. & Arnaud, A., 1995. Deflation of Mount Etna monitored by spaceborne radar interferometry, *Nature,* **375,** 567–570.

Massonnet, D., Holzer, T. & Vadon, H., 1997. Land subsidence caused by East Mesa geothermal field, California, observed using SAR interferometry, *Geophys. Res. Lett.,* **24,** 901–904.

Menke, W., 1984. *Geophysical Data Analysis: Discrete Inverse Theory,* Academic Press, Orlando.

Mitchell, A.R. & Griffiths, D.F., 1980. *The Finite Difference Method in Partial Differential Equations,* Wiley, New York.

Mogi, K., 1958. Relations between the eruptions of various volcanoes and the deformations of the ground surfaces around them, *Bull. Earthq. Res. Inst.,* **36,** 99–134.

Moore, J.N., Adams, M.C., Bishop, B.P. & Hirtz, P., 1989. A fluid flow model of the Coso geothermal system: Data from production fluids and fluid inclusions, 14th Workshop on Geothermal Reservoir Engineering, pp. 139–144, Stanford University.

Mossop, A. & Segall, P., 1999. Volume strain within The Geysers geothermal field, *J. geophys. Res.,* **104,** 29 113–29 131.

Murakami, M., Tobita, M., Saito, T. & Masharu, H., 1996. Coseismic crustal deformations of the 1994 Northridge, California earthquake detected by interferometric analysis of SAR images acquired by the JERS-1 satellite, *J. geophys. Res.,* **101,** 8605–8614.

Parker, R.L., 1994. *Geophysical Inverse Theory,* Princeton University Press, Princeton.

Plouff, D. & Isherwood, W.F., 1980. Aeromagnetic and gravity surveys in the Coso Range, California, *J. geophys. Res.,* **85,** 2491–2501.

Pratt, R.G. & Chapman, C.H., 1992. Traveltime tomography in anisotropic media—II. Application, *Geophys. J. Int.,* **109,** 20–37.

Reasenberg, P., Ellsworth, W. & Walter, A., 1980. Teleseismic evidence for a low-velocity body under the Coso geothermal area, *J. geophys. Res.,* **85,** 2471–2483.

Remy, F., Shaeffer, P. & Legresy, B., 1999. Ice flow physical processes derived from the ERS-1 high-resolution map the Antarctica and Greenland ice sheets, *Geophys. J. Int.,* **139,** 645–656.

Ridgway, J.R., Minster, J.B., Williams, N., Bufton, J.L. & Krabill, W.B., 1997. Airborne laser altimeter survey of Long Valley, California, *Geophys. J. Int.,* **131,** 267–280.

Roquemore, G., 1980. Structure, tectonics and stress field of the Coso Range, Inyo County, California, *J. geophys. Res.,* **85,** 2434–2440.

Sanders, C., Ho-Liu, P., Rinn, D. & Kanamori, H., 1988. Anomalous shear wave attenuation in the shallow crust beneath the Coso volcanic region, California, *J. geophys. Res.,* **93,** 3321–3338.

Singh, S.J., 1970. Static deformation of a multilayered half-space by internal sources, *J. geophys. Res.,* **75,** 3257–3263.

Smith, I.M., 1982. *Programming the Finite Element Method with Applications to Geomechanics,* John Wiley and Sons, Chichester.

Stakgold, I., 1979. *Green's Functions and Boundary Value Problems,* John Wiley and Sons, Chichester.

Tarantola, A., 1987. *Inverse Problem Theory: Methods for Data Fitting,* Elsevier, Amsterdam.

Vadon, H. & Sigmundsson, F., 1997. 1992–1995 Crustal deformation at Mid-Atlantic ridge, SW Iceland, mapped by radar interferometry, *Science,* **275,** 193–197.

Vasco, D.W., Johnson, L.R. & Goldstein, N.E., 1988. Using surface displacement and strain observations to determine deformation at depth, with an application to Long Valley Caldera, California, *J. geophys. Res.,* **93,** 3232–3242.

Vasco, D.W., Smith, R.B. & Taylor, C.L., 1990. Inversion for sources of crustal deformation and gravity change at the Yellowstone Caldera, *J. geophys. Res.,* **95,** 19 839–19 856.

Vasco, D.W., Karasaki, K. & Myer, L., 1998. Monitoring of fluid injection and soil consolidation using surface tilt measurements, *J. Geotech. Geoenv. Eng.,* **124,** 29–37.

Vasco, D.W., Johnson, L.R. & Marques, O., 1999. Global Earth structure: Inference and assessment, *Geophys. J. Int.,* **137,** 381–407.

Vasco, D.W., Karasaki, K. & Doughty, C., 2000. Using surface deformation to image reservoir dynamics, *Geophysics,* **65,** 132–147.

Walck, M.C., 1988. Three-dimensional V_p/V_s variations for the Coso region, California, *J. geophys. Res.,* **93,** 2047–2052.

Walck, M.C. & Clayton, R.W., 1987. P wave velocity variations in the Coso region, California, derived from local earthquake travel times, *J. geophys. Res.,* **92,** 393–405.

Walter, A.W. & Weaver, C.S., 1980. Seismicity of the Coso Range, California, *J. geophys. Res.,* **85,** 2441–2458.

Wicks, C., Jr., Thatcher, W. & Dzurisin, D., 1998. Migration of fluids beneath Yellowstone caldera inferred from satellite radar interferometry, *Science,* **282,** 458–462.

Wright, L.A., 1976. Late Cenozoic fault patterns and stress fields in the Great Basin and westward displacement of the Sierra Nevada block, *Geology,* **4,** 489–494.

Wright, C.A., Davis, E.J., Minner, W.A., Ward, J.F., Weijers, L., Schell, E.J. & Hunter, S.P., 1998. Surface tiltmeter fracture mapping reaches new depths —10,000 feet and beyond?, *SPE,* **39919,** 1–12.

Wu, H. & Lees, J.M., 1999. Three-dimensional *P* and, *S* wave velocity structures of the Coso Geothermal Area, California, from microseismic travel time data, *J. geophys. Res.,* **104,** 13 217–13 233.

Young, C. & Ward, R.W., 1980. Three-dimensional Q^{-1} model of the Coso Hot Springs known geothermal resource area, *J. geophys. Res.,* **85,** 2459–2470.

Zebker, H.A. & Goldstein, R.M., 1986. Topographic mapping from interferometric synthetic aperture radar observations, *J. geophys. Res.,* **91,** 4993–4999.

Zebker, H.A., Rosen, P.A., Goldstein, R.M., Gabriel, A. & Werner, C.L., 1994. On the derivation of coseismic displacement fields using differential radar interferometry: The Landers earthquake, *J. geophys. Res.,* **99,** 19 617–19 634.

APPENDIX A: RESOLUTION AND COVARIANCE ESTIMATION

Our model parameter estimates are based upon a singular value decomposition (SVD) of **G**. That is, the representation of **G** as the product

$$\mathbf{G} = \mathbf{U}\mathbf{\Lambda}\mathbf{V}^{\mathrm{T}}, \tag{A1}$$

where $\mathbf{\Lambda}$ is a diagonal matrix of singular values and the matrices **U** and **V** satisfy the orthogonality relations $\mathbf{U}^{\mathrm{T}}\mathbf{U} = \mathbf{I}$ and $\mathbf{V}^{\mathrm{T}}\mathbf{V} = \mathbf{I}$ Golub & Van Loan (1989). As outlined here, the resolution and covariance follow directly from the SVD of **G**. Once the decomposition is performed, it is a relatively straightforward matter to examine the trade-off between model parameter resolution and uncertainty, based upon a cut-off of singular values. There is an efficient iterative algorithm, rooted in a three-term recursion proposed by Lanczos (1950), for constructing a partial SVD. This technique is applicable to very large inverse problems Vasco *et al.* (1999), problems which are simply too big to reside in core memory.

The relative sizes of the elements λ_i provide a direct measure of the singularity of the problem Golub & Van Loan (1989). One way to regularize an inverse problem is to form a truncated representation of **G**. In the truncated representation, the column vectors of **V** and **U** associated with small elements of $\mathbf{\Lambda}$ are ignored. That is, a representation of the form eq. (A1), based only on the singular vectors associated with values of λ_i which are deemed to be significantly different from zero. The truncated representation, in which only *p* singular values and singular vectors are retained, is written $\mathbf{U}_p\mathbf{\Lambda}_p\mathbf{V}_p^{\mathrm{T}}$. The generalized inverse of **G** is written in terms of the truncated representation

$$\mathbf{G}^{\dagger} = \mathbf{V}_p\mathbf{\Lambda}_p^{-1}\mathbf{U}_p^{\mathrm{T}} \tag{A2}$$

and the model parameter estimates are given by

$$\hat{v} = \mathbf{V}_p\mathbf{\Lambda}_p^{-1}\mathbf{U}_p^{\mathrm{T}}\mathbf{T} \tag{A3}$$

Menke (1984).

It must be emphasized that we are forming the generalized inverse of the augmented matrix **G** in eq. (25). The presence of the additional equations such as those associated with the roughness penalty will act to shape or filter the spectrum of the original matrix Γ. As noted by (Pratt & Chapman 1992), in the presence of smoothing, the estimates will contain contributions from the singular vectors of the null space of the unconstrained problem. The conventional SVD representation of the resolution matrix as $\mathbf{V}_p\mathbf{V}_p^{\mathrm{T}}$ is restricted to a damped least-squares solution (Pratt & Chapman 1992). In this Appendix we present a generalization to non-diagonal regularization terms, such as those associated with roughness penalties.

Formally, resolution is a relationship between the model parameter estimates and a hypothetical 'true' model, $\boldsymbol{\nu}$. It may be derived directly from the estimated solution, $\hat{v}$, as given by eq. (A3):

$$\hat{v} = \mathbf{V}_p\mathbf{\Lambda}_p^{-1}\mathbf{U}_p^{\mathrm{T}}\mathbf{T}. \tag{A4}$$

From the fact that $\mathbf{d} = \Gamma\nu$ and eq. (26) we have

$$\hat{v} = \mathbf{V}_p\mathbf{\Lambda}_p^{-1}\mathbf{U}_p^{\mathrm{T}} \begin{bmatrix} \Gamma \\ \mathbf{0} \end{bmatrix} \nu. \tag{A5}$$

The resolution matrix **R** is defined as the matrix

$$\mathbf{R} = \mathbf{V}_p\mathbf{\Lambda}_p^{-1}\mathbf{U}_p^{T} \begin{bmatrix} \Gamma \\ \mathbf{0} \end{bmatrix}, \tag{A6}$$

relating $\hat{v}$ to $\boldsymbol{\nu}$. Some degree of simplification is afforded by considering the SVD

$$\mathbf{G} = \begin{bmatrix} \Gamma \\ \mathbf{L} \end{bmatrix} = \mathbf{U}\mathbf{\Lambda}\mathbf{V}^{\mathrm{T}} \tag{A7}$$

in a partitioned form. In particular, the matrix **U** is written

$$\mathbf{U} = \begin{bmatrix} \mathbf{U}_1 \\ \mathbf{U}_2 \end{bmatrix}, \tag{A8}$$

where the vectors $\mathbf{U}_1$ correspond to the *N* data rows (associated with Γ) and $\mathbf{U}_2$ correspond to the *M* regularization rows (associated with **L**). Based upon the partition eq. (A8), we have the representation

$$\Gamma = \mathbf{U}_1\mathbf{\Lambda}\mathbf{V}^{\mathrm{T}} \tag{A9}$$

and the resolution matrix takes the form

$$\mathbf{R} = \mathbf{V}_p\mathbf{\Lambda}_p^{-1}\mathbf{U}_{1p}^{\mathrm{T}}\mathbf{U}_{1p}\mathbf{\Lambda}_p\mathbf{V}_p^{\mathrm{T}}. \tag{A10}$$

Because the columns of $\mathbf{U}_1$ contain only part of the singular vectors $\mathbf{U}_i$ they are not necessarily orthogonal. However, by the orthogonality of the singular vectors $\mathbf{U}_i$ we do have

$$\mathbf{U}^{\mathrm{T}}\mathbf{U} = \begin{bmatrix} \mathbf{U}_1^{\mathrm{T}} & \mathbf{U}_2^{\mathrm{T}} \end{bmatrix} \begin{bmatrix} \mathbf{U}_1 \\ \mathbf{U}_2 \end{bmatrix} = \mathbf{I}. \tag{A11}$$

Thus, we may write the product of the $\mathbf{U}_1$ matrices in terms of $\mathbf{U}_2$ and its transpose

$$\mathbf{U}_1^{\mathrm{T}}\mathbf{U}_1 = \mathbf{I} - \mathbf{U}_2^{\mathrm{T}}\mathbf{U}_2. \tag{A12}$$

The advantage of equation (A12) is in the relative sizes of the matrices $\mathbf{U}_1$ and $\mathbf{U}_2$. The array $\mathbf{U}_1$ has dimensions $N \times M_r$ where M_r is the rank of **U** while array has dimensions $M \times M_r$. Typically, we have many more data *N* than model parameters *M*. This is particularly true with InSAR data sets which are composed of hundreds of thousands range change values. A further advantage is in the

sparsity of **L** which is a finite difference operator with only a few non-zero elements per row. Thus, we can efficiently compute $\mathbf{U}_2$ from the columns of **V** and the singular values $\mathbf{\Lambda}$, using

$$\mathbf{L}\mathbf{v}_i = \lambda_i \mathbf{u}_{2i} \tag{A13}$$

Aki & Richards (1980). Using eq. (A12) the expression for the resolution matrix becomes

$$\mathbf{R} = \mathbf{V}_p \Upsilon \mathbf{V}_p^{\mathrm{T}}, \tag{A14}$$

where

$$\Upsilon = \mathbf{I} - \mathbf{\Lambda}_p^{-1} \mathbf{U}_{2p}^{\mathrm{T}} \mathbf{U}_{2p} \mathbf{\Lambda}_p. \tag{A15}$$

A1 The covariance matrix

Similar considerations lead to the construction of the model parameter covariance matrix. The derivation of the model parameter covariance matrix is based upon the fact that the model parameter estimates, $\hat{v}$ are linearly related to the data **d** as seen in equation (A4). If we use the partitioned form of **U**, as in (A8), we may write

$$\hat{v} = \mathbf{V}_p \mathbf{\Lambda}_p^{-1} \mathbf{U}_{1p}^{\mathrm{T}} \mathbf{d} = \mathbf{G}^{\dagger} \mathbf{d} \tag{A16}$$

where $\mathbf{G}^{\dagger}$ is the generalized inverse. Given this linear relationship we may relate the covariance associated with the data, $\mathbf{C}_d$, to the covariance of the model parameters, $\mathbf{C}_m$,

$$\mathbf{C}_m = \mathbf{G}^{\dagger} \mathbf{C}_d (\mathbf{G}^{\dagger})^{\mathrm{T}}. \tag{A17}$$

We shall assume that the problem has been scaled, that every row has been normalized by the standard error of the associated datum (see eqs 18 and 19). Then $\mathbf{C}_d$ takes the form **I**. Thus,

$$\mathbf{C}_m = \mathbf{G}^{\dagger} (\mathbf{G}^{\dagger})^{\mathrm{T}}, \tag{A18}$$

or, in terms of the SVD of **G**,

$$\mathbf{C}_m = \mathbf{V}_p \mathbf{\Lambda}_p^{-1} \mathbf{U}_{1p}^{\mathrm{T}} \mathbf{U}_{1p} \mathbf{\Lambda}_p^{-1} \mathbf{V}_p^{\mathrm{T}} \tag{A19}$$

or

$$\mathbf{C}_m = \mathbf{V}_p \Omega \mathbf{V}_p^{\mathrm{T}}, \tag{A20}$$

where we have made use of eq. (A11), and

$$\Omega = \mathbf{\Lambda}_p^{-2} - \mathbf{\Lambda}_p^{-1} \mathbf{U}_{2p}^{\mathrm{T}} \mathbf{U}_{2p} \mathbf{\Lambda}_p^{-1}. \tag{A21}$$